Additive Manufacturing 36 (2020) 101672

Contents lists available at ScienceDirect

Additive Manufacturing

journal homepage: www.elsevier.com/locate/addma

Research Paper

Thin-wall effects and anisotropic deformation mechanisms of an additively manufactured Ni-based superalloy

Cheng-Han Yu [a,*], Ru Lin Peng [a], Vladimir Luzin [b,c], Maximilian Sprengel [d], Mattias Calmunger [a], Jan-Erik Lundgren [e], Håkan Brodin [e], Arne Kromm [d], Johan Moverare [a]

[a] Department of Management and Engineering, Division of Engineering Materials, Linköping University, Linköping SE-58183, Sweden
[b] Australian Nuclear Science and Technology Organization (ANSTO), Lucas Heights, NSW 2234, Australia
[c] School of Engineering, The University of Newcastle, Callaghan, NSW 2308, Australia
[d] Bundesanstalt für Materialforschung und -prüfung (BAM), Unter den Eichen 87, Berlin 12205, Germany
[e] Siemens Energy AB, Finspång SE-61231, Sweden

ARTICLE INFO

Keywords:
Hastelloy X
Hot tensile test
Crystallographic texture
Roughness
Residual stress
Dislocation density

ABSTRACT

Laser powder bed fusion (LPBF) of Ni-based superalloys shows great potential for high temperature applications, for example, as a burner repair application for gas turbines where the thin-walled structure is important. It motivates this work to investigate the evolution of microstructure and the anisotropic mechanical behavior when plate-like specimens are built with a thickness from 4 mm down to 1 mm. By performing texture analysis using neutron diffraction, a clear transition in fiber texture from <011> to <001> is indicated when the specimen becomes thinner. The residual stress shows no thickness dependence, and at the subsurface the residual stress reaches the same level as the yield strength. Due to the rough as-built surface, a roughness compensation method for mechanical properties of thin-walled structures is outlined and demonstrated. Tensile tests from room temperature up to 700 °C have been carried out. Anisotropic mechanical behavior is found at all temperatures, which is strongly related to the anisotropic texture evolution. Stronger texture evolution and grain rotations are discovered when the tensile loading is applied along the building direction. The mechanical behavior has been compared to a wrought material, where the high dislocation density and the subgrain structure of the LPBF material result in a higher yield strength. Combining the statistical texture analysis by neutron diffraction with mechanical testing, EBSD grain orientation mapping and the investigation of dislocation structures using transmission electron microscopy, this work illustrates the significance of texture for the thin-wall effect and anisotropic mechanical behavior of LPBF materials.

1. Introduction

Additive manufacturing (AM) has attracted significant attention in recent years for various applications in virtue of the potential advantage of product design freedom, and AM has evolved from prototyping toward practical component fabrication as techniques have progressed. Among the various material groups and techniques for AM [1], this study investigates the Ni-based superalloy manufactured by laser powder bed fusion (LPBF), which is a material group with excellent high-temperature mechanical properties and corrosion resistance for gas turbine applications [2]. A solid solution strengthened alloy Hastelloy X (HX) is chosen for this work since it is a relatively easily printable material grade with almost fully dense as-built microstructure [3]. A specific application of LPBF HX in gas turbines is the burner repair, where the damaged burner tip is removed and the repair part is built directly onto the remaining burner [4]. The geometrical designs of components in gas turbines are rather complicated, but there is a wish to reduce the amount of material since it is directly related to the cost of the part. Therefore, a purpose of this study is to investigate the mechanical behavior when a certain dimension is close to its minimum limit. As a typical repair procedure, no post-treatment such as hot isostatic pressing or rough surface machining is applied, so the studied specimens are in the as-built condition in this work.

For the thin-walled structure, the roughness of the as-built surface becomes critical, acting as a stress concentration for crack initiation and influencing the net cross-section area that determines the load carrying

* Corresponding author.
E-mail address: cheng-han.yu@liu.se (C.-H. Yu).

https://doi.org/10.1016/j.addma.2020.101672
Received 24 June 2020; Received in revised form 15 September 2020; Accepted 14 October 2020
Available online 22 October 2020

capacity during the tensile test [5,6]. The irregular surface morphology, such as semi-melted or unmelted powder and the melt pool structure, makes accurate surface roughness measurement difficult and often unreproducible. For instance, the method of using the focus variation and confocal microscopy addresses the difficulty of identifying different reflection conditions. For quantitative analysis and standardized comparison of surface roughness, the stylus-based profile measurement is a predominant technique even though it is two-dimensionally limited [7]. Of the various surface roughness parameters received from the measurement, it is unclear which parameter relates directly to the mechanical properties. Hence, this work will determine the effective roughness parameter via a comparison between mechanical properties and microstructure.

Due to the high thermal gradient induced by the focused laser energy input and laser scanning velocity, the rapid cooling in the LPBF process leads to high residual stresses (RS), as reported for different materials [8,9]. A heterogeneous distribution of RS in a curved thin-walled structure due to LPBF was found in the work of An et al. [10], exhibiting high tensile RS along the building direction (BD) at the thin edge of the samples, at which the value is higher than the yield strength [11]. RS mapping of Ni-based superalloys has been carried out by neutron diffraction with the resolution in mm scale [12,13], revealing tensile RS close to the surface and compressive RS in the bulk. Since RS might influence the mechanical response, the surface and subsurface RS will be investigated in this study using a depth profile with step sizes in the μm scale.

The directional energy input and rapid cooling rate for the powder bed fusion process lead to columnar grains and subgrains structure [14], which also result in a specific solidification texture along the building direction (BD) [15]. However, the multiple parameters in the powder bed fusion process can cause different texture results, and a strong <001> texture component along the BD is commonly found in electron beam melting (EBM), while the texture along the BD for LPBF materials has been reported differently [10,12,16–20]. Different scanning strategies and scan rotation have been shown to have a great influence on the texture and the anisotropic mechanical properties. In general, the standard 67° scan rotation involves a shift in the center of rotation and shows great randomness of heat flow and grain structure, relatively isotropic mechanical properties, and grain refinement [21]. Therefore, the thin-walled specimens were built with the standard 67° scan rotation for the purpose of observing geometric effects of the thin-walled structures.

Materials manufactured by powder bed fusion usually exhibit anisotropic mechanical behavior, where the mechanical strength along the BD is lower than for the other normal directions [16,17]. The columnar grain structure is responsible for the anisotropic mechanical properties, where higher dislocation density at the subgrain boundaries can act as a slip resistance barrier [22], and a relatively higher stress concentration at the grain boundaries is found when the loading direction is perpendicular to the building direction [23]. Meanwhile, the crystallographic texture formed from the nature of the powder bed fusion process also contributes to the anisotropic mechanical properties due to the discrete distribution of slip systems in the crystal structure, which can be characterized by the Taylor factor [24]. The dislocation-precipitation interaction is also a phenomenal strengthening mechanism in Ni-based superalloys at intermediate temperatures [25]. However, since HX is mainly a solid solution strengthened alloy, and our studied temperature range is outside the precipitation formation region of M_6C, $M_{23}C$, σ and μ in the time-temperature-transformation diagram [26], it is assumed that the influence of precipitation on the anisotropic deformation mechanism at elevated temperatures is negligible.

The main objectives of the present investigation are to reveal the evolution of microstructure and anisotropic mechanical behavior when it comes to thin-walled structures. Plates with different thicknesses from 1 mm up to 4 mm were therefore built. In contrast to other studies of anisotropic mechanical properties, the tensile specimens with different loading direction relative to the BD were taken from the same plate-like component in this study, so the issue of different levels of distortion between horizontally and vertically building can be minimized [27,28]. The process parameters are closely related to the microstructure and mechanical properties [21,29,30], and in order to generate results that are as generic as possible for LPBF materials, the material was printed by EOS M290 with the standard parameters, which is a commonly used equipment for LPBF. Therefore, the geometric effect on the thin-walled microstructure will be stressed in this study, and the influence of the crystallographic texture and elongated grain structure from LPBF on the anisotropic mechanical behavior will be discussed.

2. Experimentation

2.1. Additive manufacturing

The plate-like components with different nominal thicknesses – 1 mm, 1.5 mm, 2 mm, 2.5 mm and 4 mm – have been built by using the standard process of LPBF in an EOS M290 machine. In each layer, the hatching was first applied, followed by two lines of contouring with a width of 150 μm. The 67° scanning rotation was used, and the layer thickness was 20 μm. The building direction, which is the layer-by-layer stacking direction, is along the plate height direction, with the coordinate system being shown in Fig. 1. The powder used for the printing was EOS NickelAlloy HX with the nominal composition shown in Table 1. The specimens for the whole study were in the as-built state, so no heat treatment or surface processing has been applied. To allow for comparison with Hastelloy X manufactured using a conventional process, a wrought HX was also introduced in this study. The composition of the wrought HX is similar to the EOS NickelAlloy HX, and it was solution annealed for 20 minutes at 1175 °C followed by water quenching.

2.2. Mechanical testing

The flat dog-bone tensile specimens with two different orientations were taken from the plate-like components by electrical discharge machining with the dimensions following ISO 6892–2, where the gauge length was 21 mm and the gauge width was 5.25 mm. One sample was defined as the Vertical tensile specimen, where the loading direction (LD) was applied along the BD, and the other was defined as the Horizontal tensile specimen, where the LD was applied in the transverse direction (TD). The tensile tests were performed with a strain rate of 10^{-3}/s at both room temperature and elevated temperature, from 400 °C to 700 °C. For each condition, one tensile test was performed. The tensile test equipment was an Instron 5582 – 100 kN universal testing machine using an Instron 7361C extensometer with a gauge length of 12.5 mm attached to the tensile specimen. The tensile

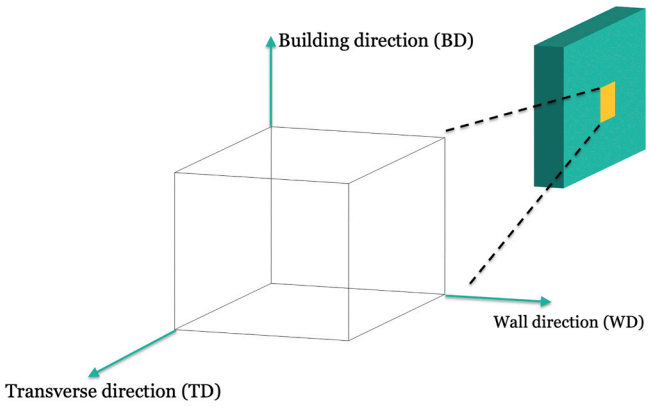

Fig. 1. The coordinate system of the sample, where the building direction (BD), wall direction (WD) and transverse direction (TD) are defined. The different thickness is the width variation on the wall direction.

Table 1
Nominal composition of EOS NickelAlloy HX, in wt%.

Ni	Cr	Fe	Mo	W	Co	C	Si
Bal.	20.5–23	17–20	8–10	0.2–1	0.5–2.5	≤ 0.1	≤ 1
Mn	**S**	**P**	**B**	**Se**	**Cu**	**Al**	**Ti**
≤ 1	≤ 0.03	≤ 0.04	≤ 0.01	≤ 0.005	≤ 0.5	≤ 0.5	≤ 0.15

specimen was placed in a heating furnace with a type K thermocouple attached to the center of the specimen to control the testing temperature, and to reach a homogeneous environment, a one-hour temperature stabilization stage was applied before each test. The same setup was applied for the wrought HX, but the tensile test was conducted on a cylindrical specimen, with the dimensions of 5 mm in diameter and 24.5 mm in parallel length.

2.3. Microstructure and texture analysis

The microstructure and grain orientation maps were investigated using a Hitachi SU 70 field emission scanning electron microscope (FE-SEM) equipped with an Oxford EBSD detector. The dislocation structures of as-built LPBF HX and wrought HX were studied by transmission electron microscopy (TEM) using an FEI Tecnai G2 microscope operating at an accelerating voltage of 200 kV. To simulate the condition at the starting point of the tensile test, LPBF HX was annealed at 700 °C for one hour to mimic the one-hour temperature stabilization stage, and then the TEM thin foil was prepared from the annealed specimen. A Struers twin-jet electropolishing system was used for the final polishing; the applied voltage was 23 V, the temperature was −25 °C, and the electrolyte was 10% perchloric acid and 90% ethanol. The melt pool structure was taken from the TEM thin foil sample under an optical microscope.

The bulk texture measurement of all as-built and deformed specimens was carried out using KOWARI, the neutron diffractometer at ANSTO [31]. The monochromatic beam with a wavelength of 1.5 Å was used to measure pole figures (PF) on an approximately 5 × 5° polar grid with cube-like samples fully emerged into neutron beam and a measurement time of 5 s per angular position. Five PFs, (111), (200), (220), (311) and (222), were obtained for each sample. An open-source MATLAB toolbox MTEX was used for the data analysis of both EBSD data and neutron diffraction pole figure data [32,33]. The Taylor factor, M, was calculated from the obtained PFs, and the axisymmetric deformation tensor was applied on different tensile loading directions with the consideration of the <011>{111} slip system [34].

To study the anisotropic deformation mechanism between the vertical and horizontal tensile tests, the specimens of 2.5 mm thickness were deformed at room temperature and 700 °C respectively in order to reveal any change in texture. The specimens were half-deformed and fully deformed respectively for the study at 700 °C while the specimens were half-deformed for the study at room temperature. The condition for the half-deformed samples corresponds to a strain chosen as 50% of the elongation at fracture depending on each test condition, and fully deformed samples refer to the fractured samples outside the necking region.

2.4. Surface roughness measurement

The surface roughness was investigated by image analysis from the cross-section of the specimen. The cross-section image was analyzed using an in-house MATLAB script [35], which generated a 2D roughness profile as schematically illustrated in Fig. 2. Roughness parameters calculated from the roughness profile include R_a (arithmetic mean values of the Z-coordinates), R_c (mean value of Zt_i in each S_i), R_z (maximum Zt_i), R_v (maximum Zv_i), R_p (mean value of Zp_i in each S_i) and R_q (root mean square of the Z-coordinates).

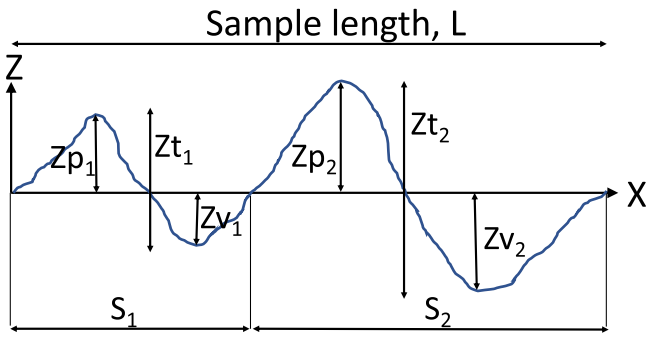

Fig. 2. Schematic illustration of the roughness profile.

2.5. Residual stress determination

The RS was determined non-destructively using a Stresstech Xstress G3 diffractometer. The $\sin^2\psi$ method was used due to the fact that laboratory X-ray sources can only penetrate the material in the order of a few micrometers. Thus, upon the assumption of a biaxial stress state, any in-plane stress component can be obtained from the slope of the linear plot of lattice spacings (d) versus sin2ψ, where ψ is the tilt angle from the sample surface normal towards the stress component direction. Further details of the method are described in [36]. The diffraction pattern was acquired using a MnKα X-ray radiation source and a 2 mm collimator. The {311} lattice plane spacings at a 2θ angle of about 156° were calculated along the 21 different tilts in the ψ angle range from −45° to +45°. The diffraction peaks were fitted using the Pearson VII function and the background was fitted with a parabolic function. The RS was subsequently calculated using a Young's modulus of 188 GPa and a Poisson ratio of 0.31, which is chosen considering values from other Ni-based superalloys found in the literature [10,12,13,37–39]. It is in accordance to the bulk Young's modulus determined from the tensile tests in this study.

The RS in the BD was determined at seven positions within the specimen gauge section with a step size of approximately 4.7 mm. The RS in the TD were probed at three positions with a step size of 7 mm. Before each measurement the distance between the specimen surface and the source was adjusted automatically to avoid any influence of specimen misalignment. Depth profiles were made next to the gauge section using a Struers MovilPol-3 electropolishing machine. Each polishing step was performed at a voltage of 20 V and the time was set to 10 s. The depth was measured using a dial indicator.

3. Results

3.1. As-built microstructure and texture

The as-built microstructure of a 1 mm thick specimen is compared between an SEM image and an EBSD grain orientation map in Fig. 3(a) and (b). A grain structure roughly elongated along the BD is representative as an overview of the as-built LPBF microstructure. Close to the surface area on both sides, some semi-melted or unmelted powder particles are shown on the outer surface, and there is no clear microstructural difference to indicate the transition from hatching to contouring during each layer printing process. Within the grains defined by high angle grain boundaries (>10°), a subgrain structure is found and indicated by low angle grain boundaries (>2°). The subgrain structure refers to the columnar dendrite arms without any secondary arms, as shown in Fig. 3(b) and (d), and the local grain growth variation of the dendrite arms is also revealed. The melt pool structure from the as-built specimen is shown in Fig. 3(c), where it can be seen that each melt pool geometry is not identical, and that the size varies from tens of micrometers to around 100 μm. As evident in Fig. 3(d), the columnar dendrite arms can grow continuously across the melt pool boundaries, and multiple grain

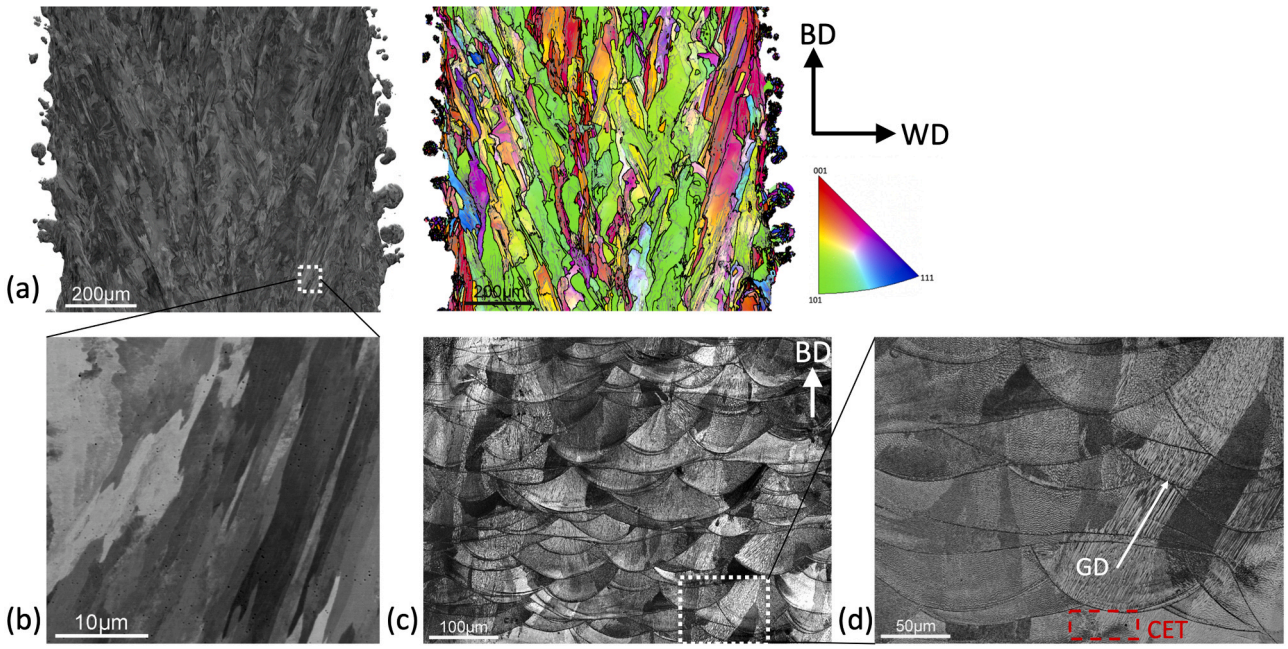

Fig. 3. (a) Microstructure of the as-built 1 mm thick specimen from an SEM image and compared with the same area from EBSD grain orientation mapping. The color legend is according to the BD; the black lines refer to $> 10°$ grain boundaries and the gray lines refer to $> 2°$ grain boundaries. (b) The microstructure from the selected area in (a). (c) The melt pool structure of the as-built specimen from the optical microscope image. (d) The melt pool microstructure from the selected area in (c), the white arrow refers to the grain growth direction (GD) and the red labeled area refers to the columnar to equiaxed transition (CET). (For interpretation of the references to color in this figure legend, the reader is referred to the web version of this article.)

growth directions (GD) of the columnar dendrite arms can exist within a melt pool. The grain growth and columnar to equiaxed transition (CET) will be further discussed in the later section.

The PFs obtained by means of neutron diffraction have been reconstructed to an orientation distribution function (ODF), and the inverse pole figures (IPF) of different thicknesses are shown in Fig. 4. A clear texture transition from the thickest sample (4 mm) to the thinnest (1 mm) is discovered along both the TD and the BD, where the 4 mm sample refers to the relative bulk texture and the 1 mm specimen reveals the thin-wall effect. Along the TD, a strong <001> texture component is observed for the 1 mm sample, and the intensity decreases for the thicker samples. Along the BD, a <011> texture component is shown in the IPF of the 4 mm sample; the intensity decreases for the thinner samples and transfers toward <001> between 2 mm and 1 mm. Based on the <011>{111} slip system in FCC crystals and an assumption of axisymmetric deformation to the loading direction, the Taylor factor, M, is calculated for vertical and horizontal deformation in each thickness, see Fig. 5. A decreasing tendency is shown for the thinner specimens, but it remains at a similar level for the 1.5 mm and 2.5 mm thick specimens. The M for the horizontal tensile direction is higher than the M for the vertical direction for all the specimens, and a larger influence of specimen thickness is found in the vertical direction.

3.2. Surface roughness

The different surface roughness parameters of each specimen are shown in Fig. 6. The surface roughness shows no correlation to thickness variation. The average R_a is 29 ± 1.8 μm, R_q is 36 ± 1.8 μm, R_v is 70 ± 3.8 μm, R_c is 101 ± 7.2 μm, R_p is 97 ± 6.6 μm and R_z is 167 ± 3.5 μm.

3.3. Residual stress

The RS measurements were carried out on both sides of the gauge section of the tensile specimens over a range of 28 mm, see Fig. 7. The center is set as the zero position and the RS was determined in the BD and the TD. The RS error for the surface measurements is below 15 MPa, which indicates that the texture effect is less pronounced on the surface concerning the different bulk texture between the two specimens. The surface RS of the 1 mm and 4 mm tensile specimens exhibit no significant difference as the values remain at a similar level along the gauge section. The RS magnitude in the BD is approximately 75 MPa higher than in the TD. The RS in the TD is close to zero, which is assumed to be due to the larger stress relaxation during the EDM process. The full-width-half-maximum (FWHM) of the measured peaks is shown in Fig. 7(c) and (d). Although the difference is within the uncertainty range, the trend of slightly higher FWHM for the 4 mm samples is clear. Similar findings are observed for the FWHM values in the TD. A higher FWHM might imply a higher dislocation density that could be caused by different cooling rates. However, the influences of microstructure or strain changes on the peak broadening are convoluted and need to be addressed in the future study. The RS depth profiles in the BD are shown in Fig. 8, where the depth direction is along the WD. For the 4 mm thick specimen, a steep rise in RS is found from the surface to around 100 μm, and after the increase, a plateau of around 537 MPa is shown, which is close to the yield strength at room temperature and surpasses the yield strength at elevated temperatures as shown in Table 2. The depth at which the plateau is reached is close to the roughness parameter R_c which refers to the average peak-valley distance of the rough surface. Hence, it could indicate that the RS at the plateau is representative of the surface RS without the influence from the semi-melted or unmelted powder particles [40]. For the depth profile of the 1 mm thick specimen, the RS values also reach at similar level as the 4 mm thick specimen at the depth around 100 μm. Since the roughness values of 1 mm and 4 mm thick specimens are at the same level, see Fig. 6, the surface RS condition between the two specimens is therefore assumed to be similar. As the measurements were carried out on the tensile specimen, a certain stress relaxation resulting from the EDM cutting needs to be considered [28]. Therefore, the actual RS values in the as-built state could be higher.

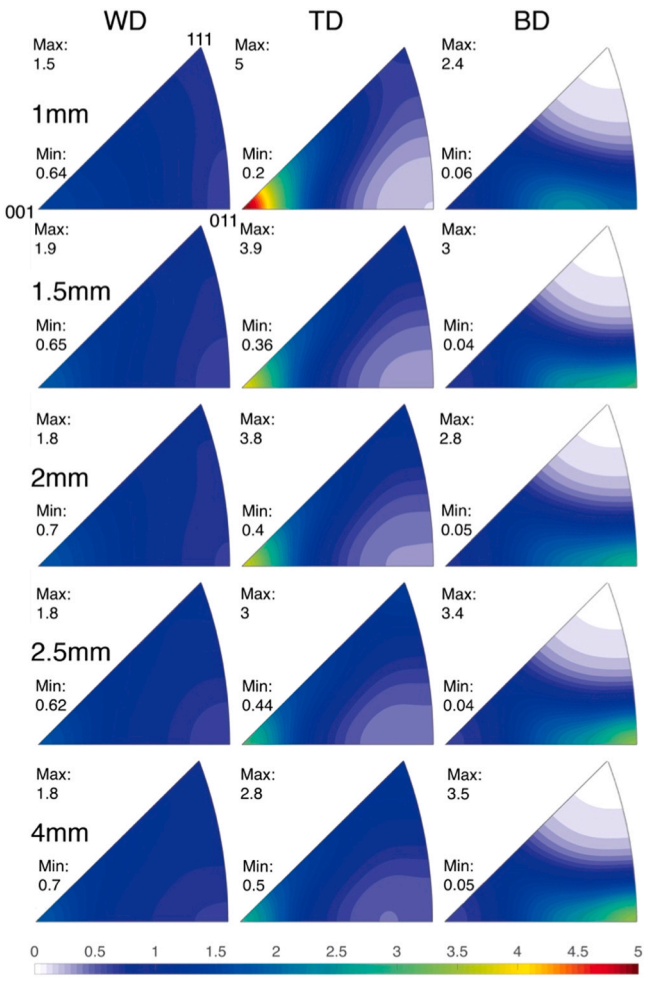

Fig. 4. Recalculated IPFs based on ODF reconstructed from neutron diffraction pole figures. The IPFs for samples with different thicknesses are shown according to the different principle directions WD, TD and BD. The maximum and minimum intensities are labeled in each IPF.

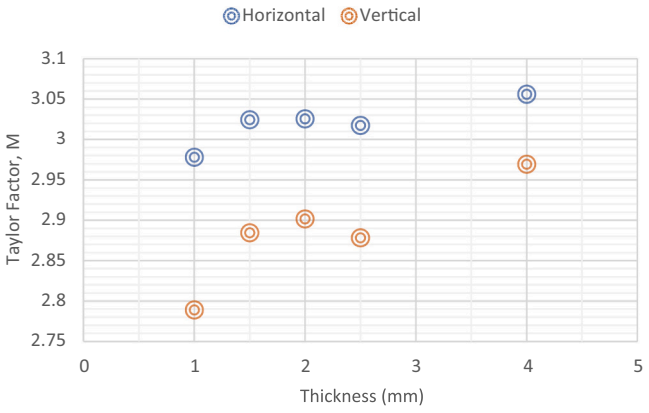

Fig. 5. Taylor factor, M, calculated from the experimental PFs. For each thickness of the specimen, M has been calculated in both vertical and horizontal tensile directions.

3.4. Mechanical properties

The tensile properties of all the tests in this study are summarized in Table 2, where the cross-section area was measured using a caliper and it refers to the outermost points of the rough surface. At each temperature,

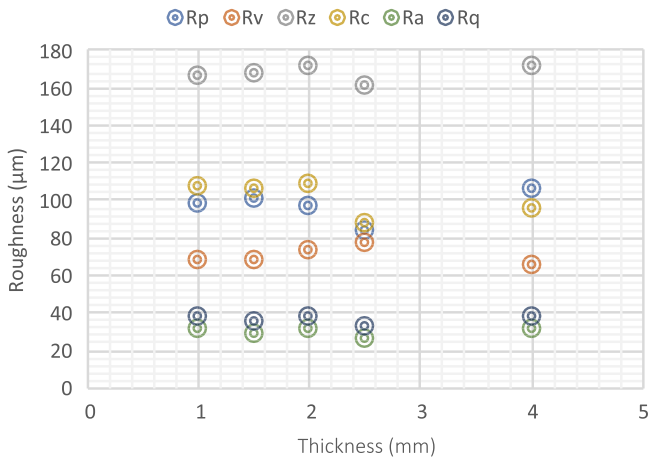

Fig. 6. Surface roughness parameters, R_a, R_q, R_v, R_c, R_p and R_z, of each specimen with different thickness.

the thinner specimen shows lower yield strength and ultimate tensile strength (UTS), and the anisotropic mechanical properties are indicated by the higher yield strength and UTS for the horizontal tests. With increasing temperatures, both the horizontal and vertical tensile strengths reveal a descending tendency. However, the elongation at fracture is approximately independent of the thickness and temperature variation between room temperature and 600 °C; the vertical elongation is 39 ± 2%, and the horizontal elongation is 27 ± 3%. At 700 °C, the vertical ductility remains at the same level, but the horizontal ductility shows a significant drop.

The comparison of the tensile behavior between LPBF and wrought Hastelloy X (HX) at 600 °C is shown in Fig. 9. The yield strength of LPBF outperforms the wrought HX, but the work hardening and the ductility of the wrought HX is much higher. For the UTS performance, only the thicker 2–4 mm horizontal specimens are at the same level as the wrought HX, while the rest are lower than the wrought HX. Among the different LPBF HX samples, the plastic behavior is similar, but the horizontal work hardening is slightly higher.

3.5. Anisotropic deformation behavior

The texture evolution of 2.5 mm thick specimen at different strain level and temperature condition is shown in Fig. 10. The vertical and horizontal tests exhibit very different deformation behaviors at both room temperature and 700 °C. The half-deformed and fully deformed texture at 700 °C is shown in Fig. 10(b). For the vertical deformation, the deformed texture becomes much weaker than the texture in the as-built state. Along the BD, the original <011> texture at the as-built state evolves towards <112> on the [001] – [111] boundary, and a minor <011> texture component forms with increased strain after half-deformation. Along the TD, the texture is close to the <011> and a weak texture along the [001] – [111] boundary is found; while along the WD, the texture close to <001> is also revealed and it becomes slightly weaker with the increased strain. On the other hand, for the horizontal deformation, a strong <001> texture component with a minor <111> texture component is discovered along the TD at the half-deformed point, and the two texture components reach the same level at the fully deformed point. Along the BD, the <011> texture component stays at the same corner, but the texture is weakened with increased strain. For the deformation behaviors at room temperature shown in Fig. 10(c), they are similar to the behaviors at 700 °C.

The microstructure of the fully deformed specimen is shown in Fig. 11. For the vertical deformation, the elongated grains and subgrains align towards the LD, and some grains that are nearly parallel to the LD have the orientation of <001>//LD (the color legend is red). However, for the horizontal deformation, the grain morphology becomes more

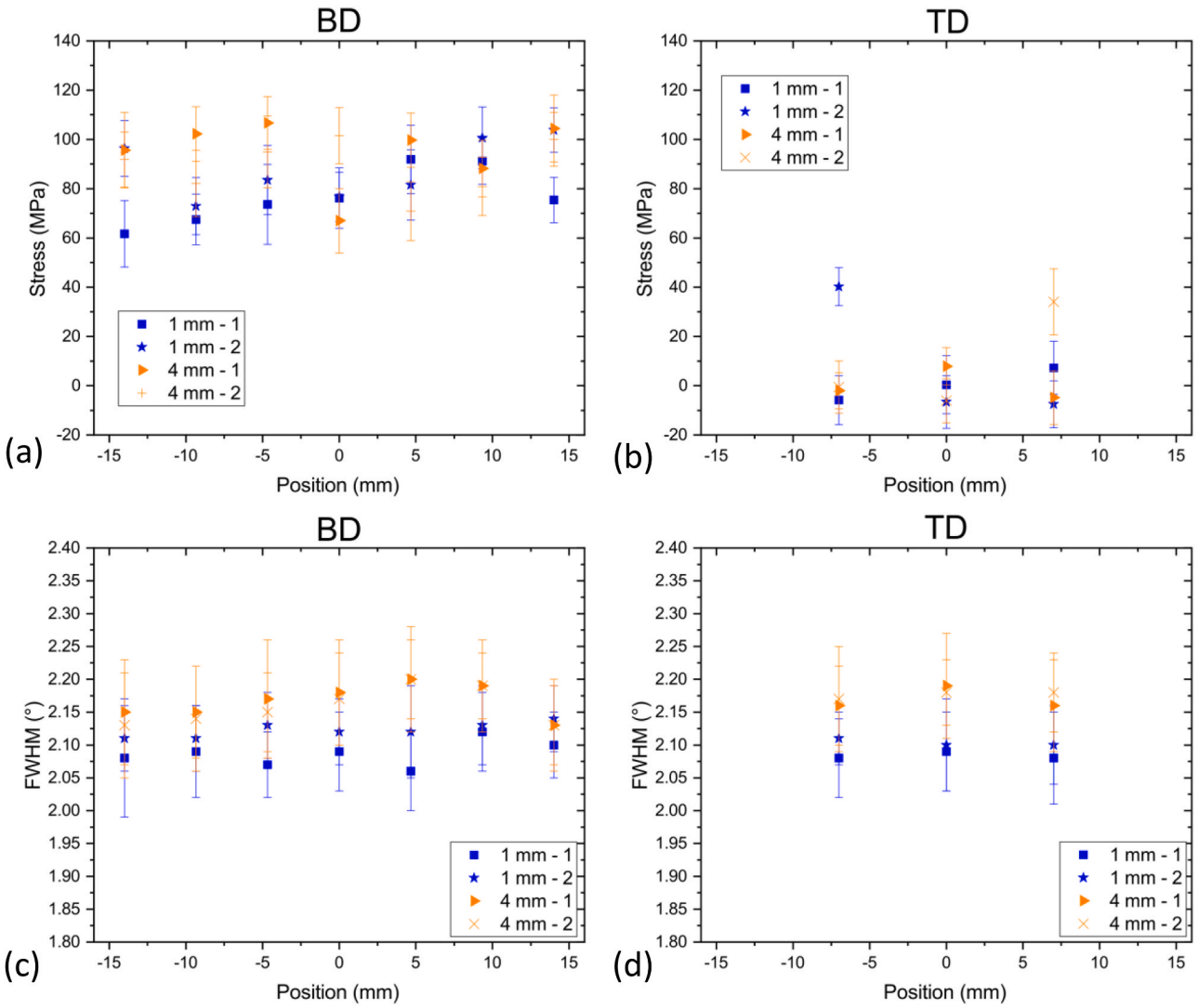

Fig. 7. RS on both sides of the surface of the 1 mm and 4 mm tensile specimens. The measurement was carried out on the center of the gauge section. The zero position denotes the center. (a) RS in the BD, where seven points were measured. (b) RS in the TD, where three points were measured. (c) FWHM of the measured 311 peaks in the BD. (d) FWHM of the measured 311 peaks in the TD.

irregular, but the major orientation of the grains still remains <011>// LD (the color legend is green).

4. Discussion

4.1. As-built microstructure and geometric influence on the different texture behaviors

The elongated grain structure with a preferred orientation as shown in Fig. 3 is commonly found in AM materials, but the texture varies with different energy input source and printing parameters [27]. In a comparison of the as-built texture between different energy input sources, it is quite common to find a strong <001> texture component along the BD in electron beam melting (EBM) materials, while the texture along the BD in LPBF materials remains unclear [16–20]. The scanning rotation of 67° applied in this work aims to promote isotropic microstructure and random texture, since the scanning rotation shows considerable influence on the solidification structure [21,41–43]. Hence, the mechanism for the texture transition with thickness variation shown in Fig. 4 is assumed to be related to the geometric constraints. The PFs of 1 mm and 4 mm thick specimens are shown and compared to the theoretical fiber textures in Table 3. For the 4 mm thick specimen, the (220) PF corresponds well with the simulated PF for <011> fiber texture while the (200) and (222) PFs are also close to the simulated PFs but with a higher deviation, so a <011> partial fiber texture along the BD can be deduced from the comparison. For the 1 mm thick specimen, the (200) PF is close to the simulated PF of <001> fiber texture; the (220) and (222) PFs match on the 45° polar angle but there is no symmetry between BD and WD on the azimuth angle, hence the PFs indicate a <001> partial fiber texture along the TD. Unlike the high temperature chamber in EBM, the powder bed in LPBF has lower temperature compared to the hatching area. When the thickness dimension decreases below a certain limit, the thermal boundary condition starts to change, and it leads the grain growth process which results in different textures.

The elongated grain and subgrain structures, as shown in Fig. 3, indicate the grain growth direction of the columnar primary dendrite arm during the solidification process. The GD of the dendrite arm follows the energy-favorable crystallographic <001> direction, and the GD is guided by the highest thermal gradient which provides the maximum driving force for solidification [44,45]. Hence, the texture differences of the different thicknesses could be traced back to the thermal field. From the Rosenthal equation [46,47], the local thermal field at the melt pool is related to the thermal diffusivity and conductivity, the absorption coefficient of the powder, the input energy density, and the laser moving

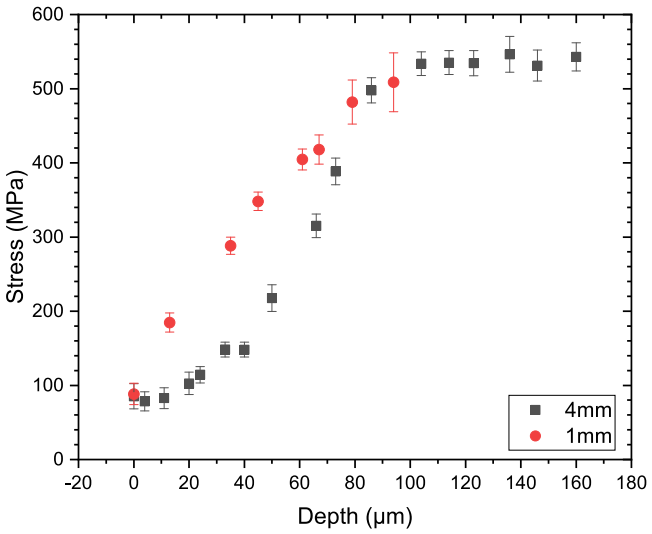

Fig. 8. Depth profiles of the RS on the grip section of the 1 mm and 4 mm tensile specimen. The RS in the BD is determined. The depth profile direction is along the WD.

speed. Based on the observation of melt pool structure shown in Fig. 3(c) and (d), a schematic illustration of the grain growth is given in Fig. 12 where different scenarios could take place within a melt pool. The nucleation sites for the dendrite arms can be, for instance, the dendrite arms that are already solidified, the melt pool boundaries, and the region of columnar to equiaxed transition of grain growth. The dendrite arms typically grow through the melt pool boundaries.

When different GDs of the dendrite arms encounter each other, they will be in a competitive relationship, and the most energy-favorable GD will dominate. The competition of preferable GDs can take place either within a melt pool or at the melt pool boundaries. The columnar dendrite arms sometimes become equiaxed, and the transition can be described by Hunt's model [44,47–49], where the ratio G^n/V determined the CET. G is the thermal gradient $G = |\nabla T|$, $V = V_b \cos\theta$ is the solidification velocity related to the laser movement V_b in the planar direction and θ is the angle between the two vectors. When the ratio G^n/V is above a critical value, columnar grain growth will occur. Otherwise, it will be equiaxed grain growth. In Fig. 3(c) and (d), columnar dendrite arms dominate and the CET takes place where dendrite arms with different GDs meet, but in general the area of equiaxed grain growth is limited.

The laser beam movement is complicated with a 67° scan rotation in this study. Each layer has been remelted multiple times since the laser energy input can melt several layers at a time, which makes the melt pool geometry irregular. The energy input at the top of each building layer creates a strong G along the BD, but the 67° scan rotation gives a high variation of G in the planar direction between the WD and TD. Therefore, the grain growth of dendrite arms is not exactly parallel to the BD. Take the BD as a reference axis, the average deviation of GDs from this axis can determine the preferred orientation along the BD. For the 4 mm thick sample, the <011> fiber texture along the BD indicates that the deviation of GDs is evenly distributed around the BD and with an average angle of 45°. However, when it comes to the 1 mm thick sample, the G along the WD will become steeper, with the consideration of the shorter distance from the hot hatching area to the cold powder bed. The G along the WD can increase to a level similar to G along the BD, and the G along the planar direction between the WD and BD becomes more isotropic. As a result, the crystallographic <001> direction points toward the TD, and a strong <001> fiber texture along the TD is discovered in the 1 mm thick specimen.

4.2. Thin-wall effects and cross-section calibration

The cross-sectional area for the calculation of yield strength and UTS in Table 2 was measured using a caliper for each specimen, and it refers to the outermost points of the rough surface. However, the nominally

Table 2
The tensile properties obtained from all the tests in this study, where the cross-section area was measured using a caliper. The elongation stands for the strain at fracture.

Test temperature	Thickness	Condition	Yield strength (MPa)	UTS (MPa)	Elongation (%)	Young's modulus (GPa)
Room temperature	1 mm	Vertical	468	596	38	153
	2 mm	Vertical	517	647	39	170
	4 mm	Vertical	551	677	42	181
	1 mm	Horizontal	518	707	25	143
	2 mm	Horizontal	582	769	24	178
	4 mm	Horizontal	617	796	29	177
400 °C	1 mm	Vertical	377	485	43	63
	2 mm	Vertical	418	533	41	46
	4 mm	Vertical	440	561	43	103
	1 mm	Horizontal	390	553	25	100
	2 mm	Horizontal	444	619	29	130
	4 mm	Horizontal	488	652	28	149
500 °C	1 mm	Vertical	366	469	39	76
	2 mm	Vertical	407	525	37	102
	4 mm	Vertical	435	549	40	135
	1 mm	Horizontal	388	532	27	67
	2 mm	Horizontal	445	598	25	104
	4 mm	Horizontal	473	635	32	131
600 °C	1 mm	Vertical	332	432	38	79
	2 mm	Vertical	353	467	36	79
	4 mm	Vertical	403	508	40	85
	1 mm	Horizontal	364	500	27	92
	2 mm	Horizontal	411	556	29	105
	4 mm	Horizontal	430	584	32	110
700 °C	1 mm	Vertical	308	380	36	74
	2 mm	Vertical	336	491	39	82
	4 mm	Vertical	357	445	39	128
	1 mm	Horizontal	338	444	18	97
	2 mm	Horizontal	375	491	19	109
	4 mm	Horizontal	401	512	18	133

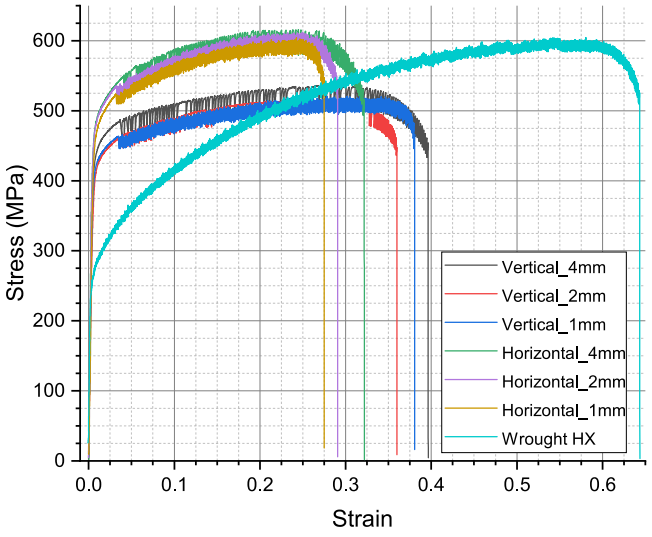

Fig. 9. A comparison of the stress-strain curves between the LPBF and the wrought Hastelloy X at 600 °C. A roughness compensation for the stress of the LPBF specimen has been applied. The compensation method will be described in a later section.

measured thickness is overestimated due to the high roughness of the as-built surface, and this will lead to a larger influence on the thinner specimens [50]. The comparison of yield strength is shown in Fig. 13, and a decreasing tendency for the thinner specimens is discovered at each test temperature. Between the 1 mm and 4 mm thick specimens, there is no significant RS difference at the surface and subsurface, up to a depth of 100 μm, see Fig. 7 and Fig. 8. Hence, a minor thickness-dependency on the surface and subsurface RS is assumed. Moreover, the FWHM between the two thicknesses remains at the same level, so the dislocation density and grain size variation are assumed to have only minor effects [51,52]. Therefore, the Taylor factor difference and the overestimated cross-section area are assumed to be the main reasons for the decreasing tendency of the yield strength. As with the cross-section shown in Fig. 3, the semi-melted or unmelted powder on the surface is the main contribution to the roughness, and this powder is assumed not to take a significant load. A method for roughness compensation that can be used to estimate the true load bearing cross-section area and true stress acting on the material is proposed as follows:

$$A_c = w \times (t - 2R) \tag{1}$$

$$\sigma_c = \frac{F}{A_c} \tag{2}$$

where A_c is the calibrated cross-sectional area, w is the width of the cross-section, t is the measured thickness using a caliper, R is the surface roughness parameter, σ_c is the calibrated yield stress and F is the loading force. After the cross-section calibration, it is assumed that only the Taylor factor difference contributes to the thin-wall effect. Assuming polycrystal deformation behavior, the Taylor factor is proportional to the yield strength [53]:

$$\sigma_c = M \times \sigma_{CRSS} \tag{3}$$

where σ_{CRSS} is the critical resolved shear stress. Since each roughness parameter is approximately constant among different thicknesses in Fig. 6, the roughness parameter for calibration can be calculated using a linear interpolation between the different thicknesses:

$$\sigma_{c,\ t_i} = \sigma_{t_i} \times \frac{A}{A_c} \tag{4}$$

$$\frac{\sigma_{c,\ t_1}}{\sigma_{c,\ t_2}} = \frac{M_{t_1}}{M_{t2}} \tag{5}$$

As a result, the calculated surface roughness parameter R is 88.6 μm, where the linear interpolation has been applied among both vertical tests and horizontal tests and for all different temperature conditions.

The calculated surface roughness parameter is close to the measured values for R_c, R_p and R_v in Fig. 6, and the calibrated yield strength with the different measured roughness parameters is shown in Fig. 13. As the roughness values are similar for different thicknesses, the calibration compensates the yield strength upwards more significantly for the 1 mm sample due to the higher portion of roughness in the cross-section. The thickness-dependence of yield strength is almost removed by the calibration with R_c. However, with the consideration of thickness-dependent Taylor factor shown in Fig. 5, it is more reasonable to choose the calibration with R_p and R_v since the yield strength is proportional to the Taylor factor. Judging from the definition of different roughness parameters shown in Fig. 2, R_p is proposed to be most suitable to use for the cross-sectional calibration. The reason is that the region above the average of the roughness profile is not expected to carry the load, so the measured roughness parameter, R_p, needs to be subtracted from the caliper-measured cross-section to obtain the true load-bearing cross-section. The cross-sectional calibration is demonstrated on the stress-strain curves in Fig. 9, where the stress for each point is modified using the roughness parameter R_p in Eqs. 1 and 2.

4.3. Mechanical behavior compared with conventional manufacturing process

The yield strength of LPBF HX is approximately 200 MPa higher than the wrought HX depending on the different thicknesses and LD, see Fig. 9. It is assumed to be related to the in-situ plastic deformation induced by the rapid cooling during the LPBF process, which can be indicated by the high dislocation density of LPBF HX shown in Fig. 14. The subgrain structure shown in Fig. 3 is also revealed in the TEM image, Fig. 14, where the width of the subgrain is around 300 nm. The dislocations pile up at the boundaries of the subgrain and the subgrain wall thickness is around 40 nm.

The yield strength difference can be analyzed by quantifying different strengthening mechanisms [54]. Since the chemical composition is similar and there is no precipitation hardening in this alloy, the strengthening mechanism could be described as:

$$\Delta\sigma_y = \Delta\sigma_{g.b.} + \Delta\sigma_{dis.} \tag{6}$$

where $\Delta\sigma_y$ is the yield strength difference between LPBF and wrought HX, $\Delta\sigma_{g.b.}$ is the grain boundaries strengthening, and $\Delta\sigma_{dis.}$ is the dislocation strengthening. $\Delta\sigma_{g.b.}$ could be described using the Hall-Petch equation:

$$\Delta\sigma_{g.b.} = \frac{k_y}{\sqrt{d}} \tag{7}$$

where k_y is the material-dependent strengthening coefficient, and d is the grain size. The grain size can be determined from the EBSD grain orientation mapping in Fig. 3 for LPBF HX and in Fig. 15 for wrought HX. Take the grain boundaries with misorientation $> 10^{\circ}$, and determine the grain size by the sectional area, which is postulated as a circle and the equivalent diameter represents the grain size. As a result, the average grain size of wrought HX is 25.6 μm, and the average of LPBF HX is 26.5 μm. The average grain sizes of both are on a similar level, so the $\Delta\sigma_{g.b.}$ is assumed to have minor contribution to the yield strength difference.

The dislocation strengthening $\Delta\sigma_{dis.}$ could be calculated by the Taylor's work hardening equation [55]:

$$\Delta\sigma_{dis.} = \alpha M G b \sqrt{\rho} \tag{8}$$

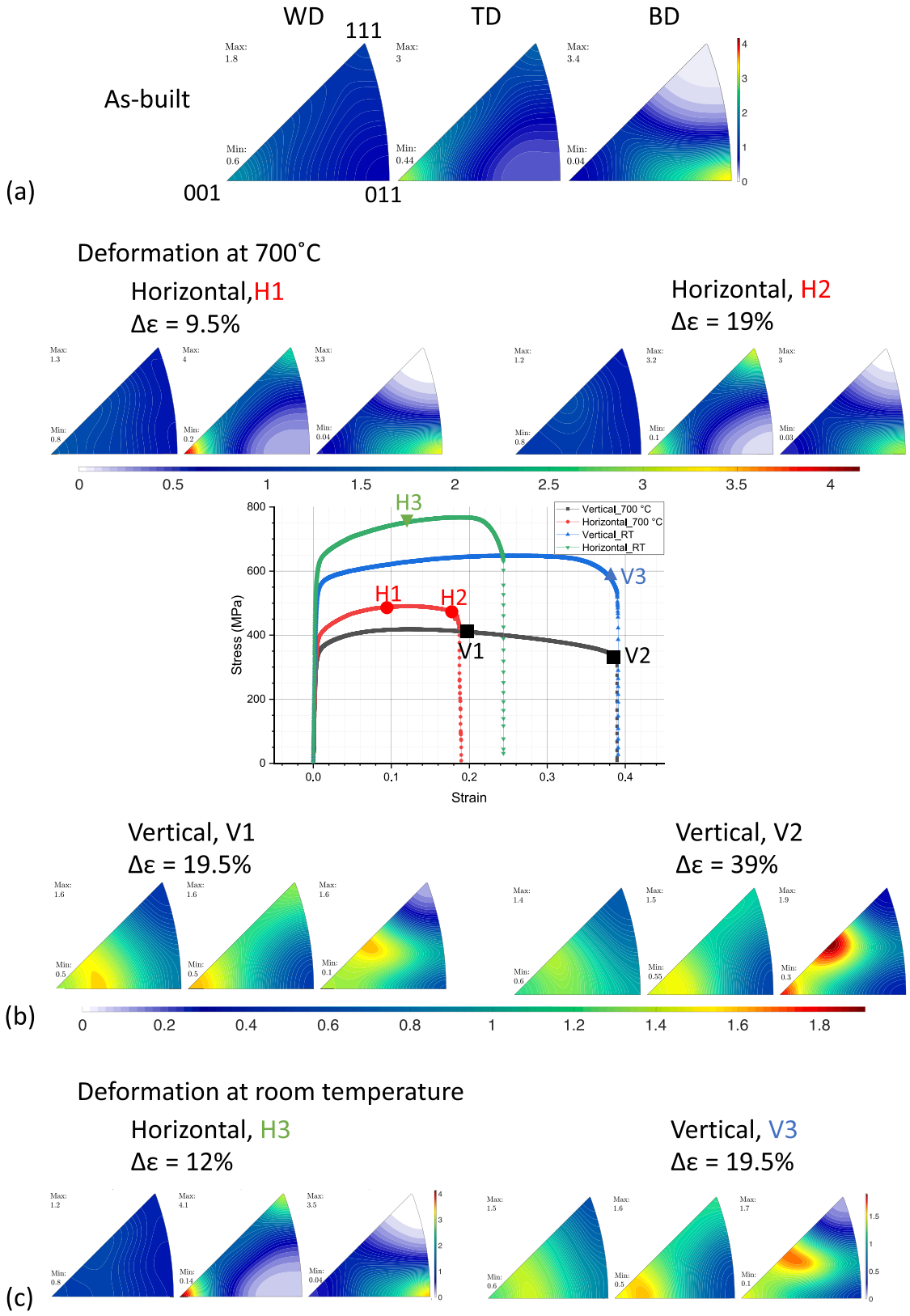

Fig. 10. The texture evolution of deformed tensile specimen at different strain level and temperature condition, in the 2.5 mm thick specimen. The IPFs are reconstructed from pole figures obtained by neutron diffraction, being presented with respect to three principle directions, WD, TD and BD. The color legends are identical in the as-built and horizontal deformation, and the vertical deformation has its own color legend due to the low intensity. (a) The as-built sample. (b) The vertical and horizontal deformation with different strain level at 700 °C. The corresponding conditions are labeled as H1, H2, H3, V1, V2 and V3 in the stress-strain curves. (c) The vertical and horizontal deformation at room temperature. (For interpretation of the references to color in this figure legend, the reader is referred to the web version of this article.)

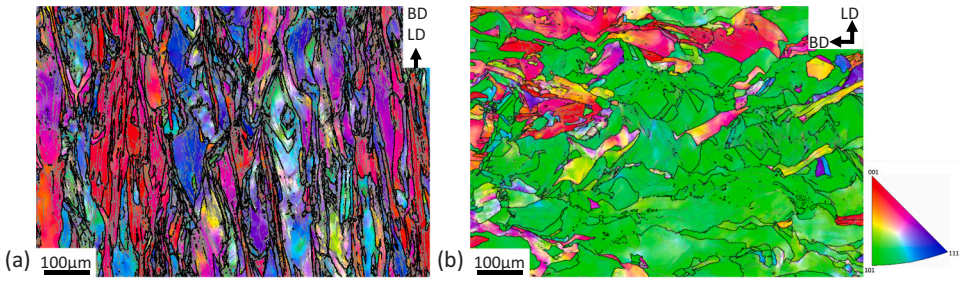

Fig. 11. EBSD grain orientation mapping of the fully deformed specimens at 700 °C. The color legend is according to each BD; the black lines refer to > 10° grain boundaries and the gray lines refer to > 2° grain boundaries. (a) The vertical tensile test. (b) The horizontal test. (For interpretation of the references to color in this figure legend, the reader is referred to the web version of this article.)

where α is a material-dependent coefficient, M is the Taylor factor as mentioned above, G is the shear modulus which could be obtained from the Young's modulus by assuming that the Poisson ratio is 0.3, b is the Burger's vector and is taken as 0.257 nm [56], and ρ is the dislocation density. For homogeneously distributed dislocations, α is set as α_{hom} = 0,47 [57]. The Taylor factor for wrought HX is isotropic, and the value is 3.03 which is calculated from the EBSD map in Fig. 15. The dislocation density can be determined by using the intersection method on the TEM images in Fig. 14 [58], and the ρ is around $5 \times 10^{12}/m^2$ for the wrought HX. However, due to the subgrain structure of LPBF, the dislocation strengthening needs to be modified where the dislocation tangling at the subgrain walls is considered [59]:

$$\Delta\sigma_{dis.} = \alpha_{het} MGb\sqrt{\rho} \tag{9}$$

$$\alpha_{het} = 2\alpha_{hom}\sqrt{f_{sub} \times f_w} \tag{10}$$

where α_{het} is the coefficient with the consideration of heterogeneous dislocation distribution, $\alpha_{hom} = 0.47$ as mentioned above, and f_{sub} and f_w are the volume fraction of subgrain and wall area. f_w is proposed as [60]:

$$f_w \approx \frac{\kappa w}{d_{sub}} \tag{11}$$

$$f_w + f_{sub} = 1 \tag{12}$$

where κ is a geometric constant taken as 3, w is the thickness of the subgrain wall, d_{sub} is the subgrain width, and f_w is calculated as 0.4 from Fig. 14. With the assumption that the major yield strength difference between LPBF HX and wrought HX comes from the dislocation strengthening $\Delta\sigma_{dis.}$, the calculated dislocation density of LPBF HX is around $2.2 \times 10^{14}/m^2$. From the dislocation structure in Fig. 14, the observed dislocation density of LPBF HX is around 10^{14}–$10^{15}/m^2$ by using the intersection method. The calculated dislocation density is close to the observed dislocation density, and it is also at a same level to other studies of Ni-based LPBF materials [61]. Therefore, it can be concluded that the high dislocation density of LPBF HX is the reason for the higher yield strength compared to wrought HX. Moreover, the partial capacity of work hardening is consumed in the as-built LPBF HX, so the ductility is worse than the wrought HX.

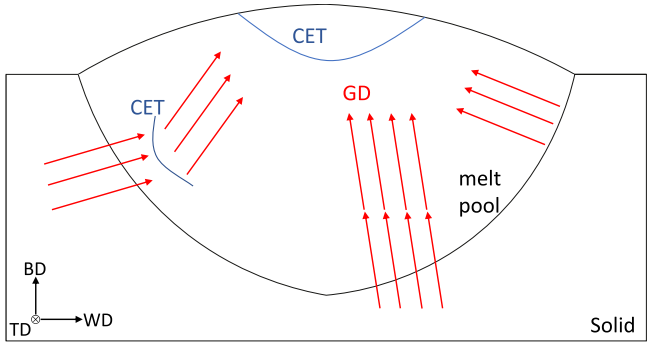

Fig. 12. Schematic of the multiple conditions of grain growth direction in a melt pool.

4.4. Anisotropic deformation mechanism

The anisotropic texture evolution is shown in Fig. 10. For the vertical tensile tests, due to the elongated grains and the <011> texture along the BD of the as-built microstructure, it can be assumed that the vertical deformation would show some similarities to deformation of a FCC single crystal with the <011> crystallographic orientation along the loading direction. The texture evolution toward the [001] – [111] boundary implies that the primary slip system is activated where the tensile axis rotates toward the <011> direction in the adjacent stereographic triangle [62]. The primary and conjugate slip systems are equally favored on the boundary, so the tensile axis will rotate toward [112] on the boundary. At the fully deformed state, the major <112>//LD and minor <001>//LD texture components along the BD correspond well with the deformed microstructure shown in Fig. 11. Most of the elongated grains are not parallel to the BD in the as-built state, but they become well-aligned along the LD and experience large lattice rotation during the plastic deformation, and these grains lead to a significant <112>//LD texture component. Meanwhile, the elongated grains that are nearly parallel to the BD in the as-built state undergo less grain rotation, and they result in the minor <001>//LD texture component. The better vertical ductility is credited with the large lattice rotation.

For the horizontal tensile tests, the deformation behaviors are close

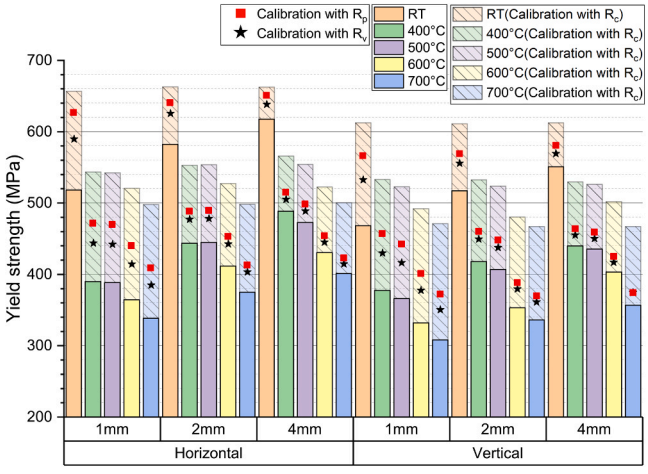

Fig. 13. The comparison between yield strengths before and after the cross-section calibration among all the tensile tests from room temperature up to 700 °C. The cross-section for the yield strength before the calibration is measured by using a caliper. The calibration refers to the subtraction of roughness value on the caliper-measured cross-section.

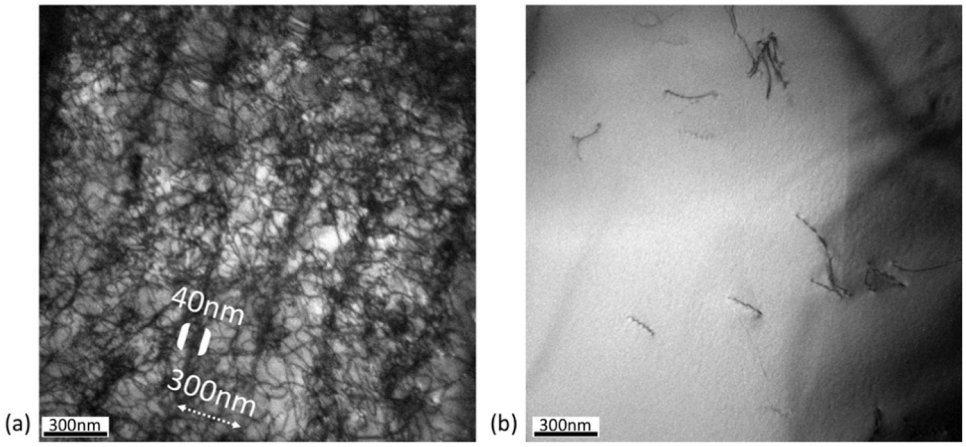

Fig. 14. Microstructural comparison between LPBF HX and wrought HX from TEM images. (a) As-built LPBF HX with 1 hour annealing at 700 °C. (b) As-received wrought HX with standard solution annealing.

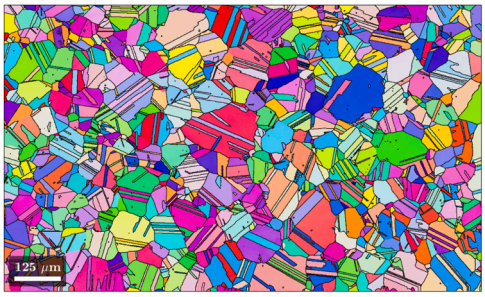

Fig. 15. EBSD grain orientation map of the wrought HX.

to polycrystalline deformation, because the preferred orientations of the deformed texture along the LD are <001> and <111>, which is the same as deformed FCC polycrystal under tension [63]. Moreover, the calculated horizontal M is around 3, which is close to the average M of 3.067 for a random texture [64], and it refers to a more isotropic mechanical behaviors. Compared to the as-built microstructure, the irregular grain boundary morphology indicates a certain level of grain rotation, but it is assumed that less rotation has been experienced due to the texture performance being similar to the as-built texture. The lower capability of grain rotation for horizontal deformation is considered to be an important reason for the lower ductility. In addition, the texture evolution behaviors are similar between 700 °C and room temperature. Yet, due to that multiple slips can be activated at high temperature, the difference between horizontal and vertical yield strength becomes smaller at 700 °C.

As a clear texture difference is shown between 1 mm and 4 mm specimen, the initial texture influences the texture evolution, see Fig. 16. For the 1 mm specimen, the strong <001>// TD texture component still remains at a certain level after vertical deformation, meanwhile, the texture evolution along the BD is similar to the 4 mm specimen that it evolves toward the [001] – [111] boundary. For the horizontal deformation, the <001>//TD texture component of 1 mm specimen become even stronger, and it does not form <111>//TD texture component like 4 mm and 2.5 mm specimen. A slightly lower degree of lattice rotation is expected in 1 mm specimen.

5. Conclusions

In this study, the effect of wall thickness of additively manufactured thin-walled structures of LPBF HX and their anisotropic plastic deformation behavior at elevated temperatures were investigated with multidisciplinary characterization techniques. Some significant conclusions are drawn as follows:

1. A clear transition of the <011> fiber texture along the BD to <001> fiber texture along the TD is shown when the specimen becomes thinner. This effect on the crystallographic texture depends on the directional energy input and the constraints on the thermal gradients caused by the geometric differences.
2. One particular result of the difference in texture is that the Taylor factor, M, decreases in the thinner walls. In addition, M is higher in the horizontal direction compared to the vertical direction, which corresponds very well with the anisotropic yield strength behavior from the tensile tests.
3. The surface roughness appears to be similar for the different thicknesses. By using a linear interpolation of the Taylor's factor and the yield strength between the different thicknesses, the roughness parameter R_p is found to be a suitable parameter for the cross-sectional calibration. The caliper-measured cross-section is subtracted by R_p to obtain the true load-bearing cross-section.
4. For the RS in the BD, a steep tensile RS gradient is shown in the depth profile along the WD. The RS reaches a plateau of about 537 MPa at the depth around 100 μm, which represents the surface RS without the influence of unmelted powder particles at the surface.
5. The high dislocation density and the dislocations piling up at the subgrain boundaries strengthen the LPBF HX. The dislocation density of LPBF HX is in the range of 10^{14}–$10^{15}/m^2$, which is generated during the rapid cooling process and is much higher than for the wrought and solution heat treated HX, which is typically $5 \times 10^{12}/m^2$. The high dislocation density of LPBF HX lowers the capacity for work hardening and reduces the ductility.
6. The deformation of the thin-walled AM samples in the vertical and horizontal directions exhibits an anisotropic behavior with characteristic texture evolution, and the deformation behavior is similar between room temperature and 700 °C. The vertical deformation has a higher degree of texture evolution and grain rotation, where the texture evolves toward the [001] – [111] boundary, which is assumed to be the main reason for higher ductility.

CRediT authorship contribution statement

Cheng-Han Yu: Conceptualization, Methodology, Validation, Investigation, Data curation, Writing - original draft, Writing - review & editing, Visualization, Project administration. **Ru Lin Peng:** Conceptualization, Methodology, Writing - review & editing, Supervision. **Vladimir Luzin:** Validation, Investigation, Resources, Data curation. **Maximilian Sprengel:** Validation, Investigation, Data curation, Writing - review & editing. **Mattias Calmunger:** Validation, Investigation. **Jan-**

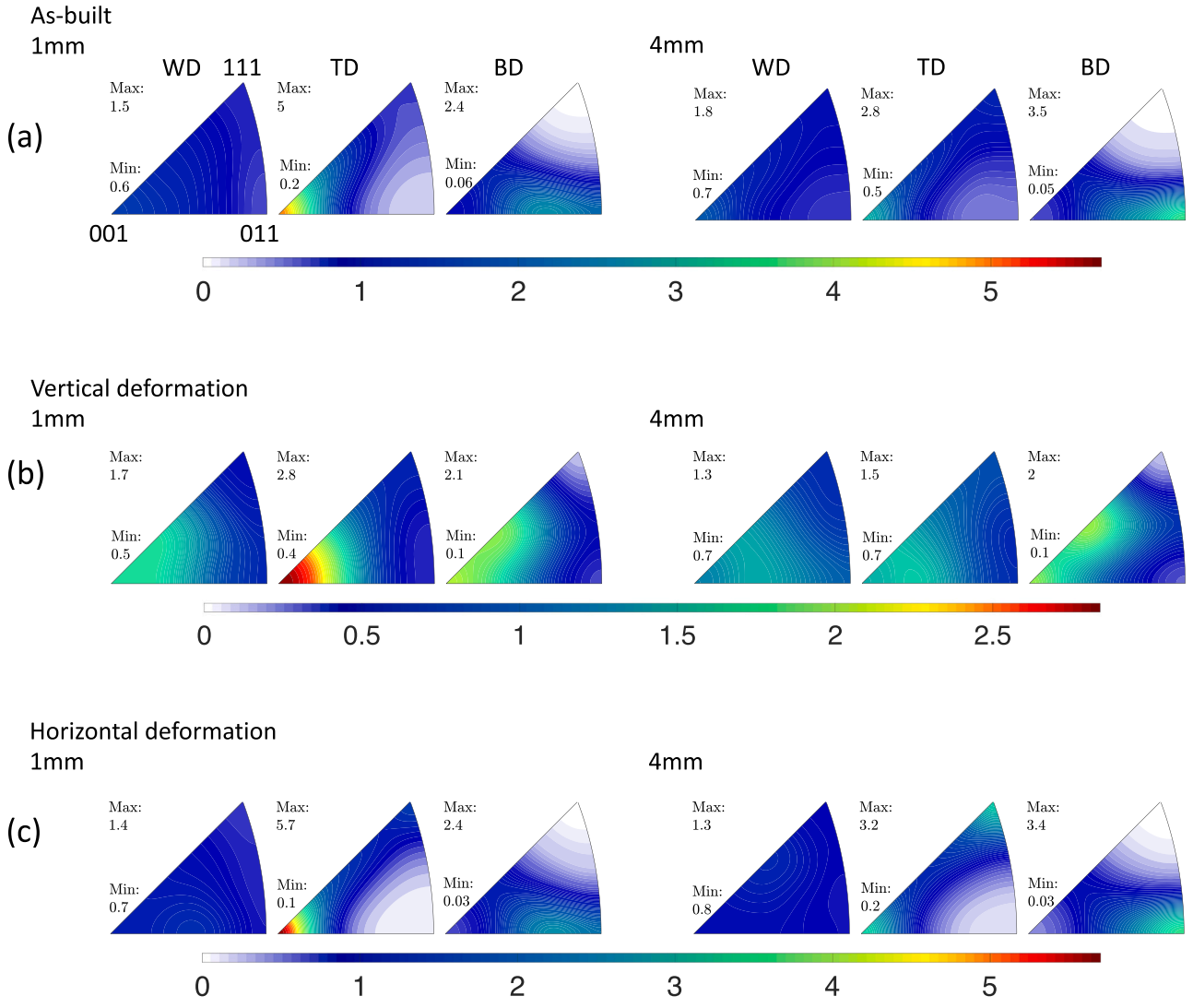

Fig. 16. The influence of initial texture on the anisotropic texture evolution at 700 °C. The texture analysis was carried out on the fully deformed samples. The color legends of as-built and horizontal deformation are identical, but the vertical deformation has its own color legend due to the low intensity. (a) The initial textures of as-built 1 mm and 4 mm specimen. (b) The vertical deformation. (c) The horizontal deformation. (For interpretation of the references to color in this figure legend, the reader is referred to the web version of this article.)

Table 3
Experimental pole figures and the comparison to the simulated <011> and <001> fiber texture.

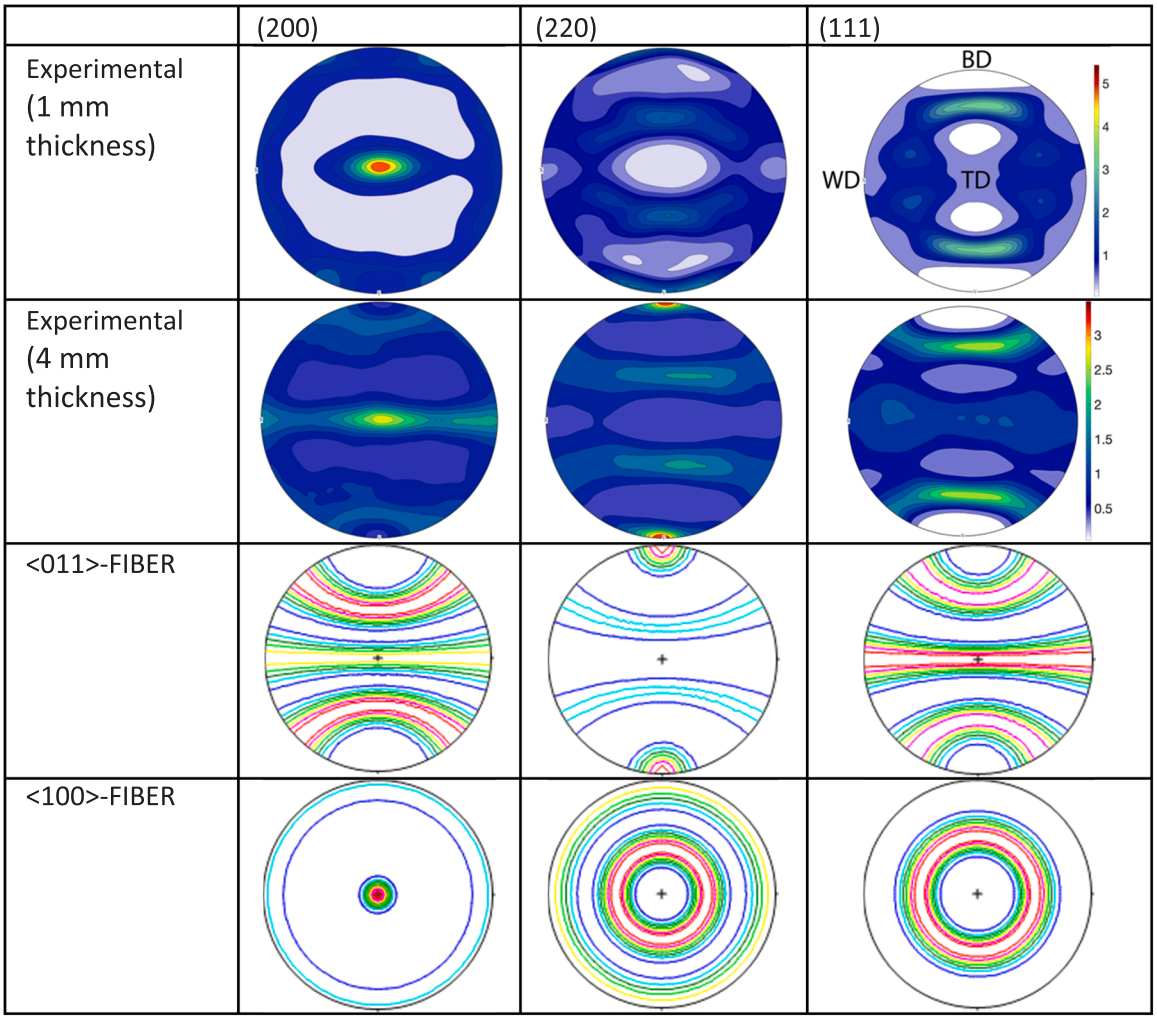

Erik Lundgren: Resources. **Håkan Brodin:** Resources. **Arne Kromm:** Investigation, Resources, Writing - review & editing. **Johan Moverare:** Conceptualization, Methodology, Resources, Writing - review & editing, Supervision, Funding acquisition.

Declaration of Competing Interest

The authors declare that they have no known competing financial interests or personal relationships that could have appeared to influence the work reported in this paper.

Acknowledgments

This study was supported by the Swedish Governmental Agency for Innovation Systems (Vinnova grant 2016-05175) and the Center for Additive Manufacturing-metal (CAM^2). Support from AFM at Linköping University and the faculty grant SFO-MATLiU#2009-00971 is also acknowledged. Gratitude is extended to Dr. R. Boyd and Dr. D. Deng for the TEM assistance.

All data included in this study are available from the corresponding author on reasonable request.

Appendix A. Supporting information

Supplementary data associated with this article can be found in the online version at doi:10.1016/j.addma.2020.101672.

References

[1] D. Bourell, J.P. Kruth, M. Leu, G. Levy, D. Rosen, A.M. Beese, A. Clare, Materials for additive manufacturing, CIRP Ann. Manuf. Technol. vol. 66 (2) (2017) 659–681.
[2] R.C. Reed, The Superalloys: Fundamentals and Applications, Cambridge University Press, 2006.
[3] W.J. Sames, F.A. List, S. Pannala, R.R. Dehoff, S.S. Babu, The metallurgy and processing science of metal additive manufacturing, Int. Mater. Rev. vol. 61 (5) (2016) 315–360.
[4] O. Andersson, A. Graichen, H. Brodin, V. Navrotsky, Developing additive manufacturing technology for burner repair, J. Eng. Gas. Turbines Power vol. 139 (3) (2016), 031506.
[5] M. Kahlin, H. Ansell, J.J. Moverare, Fatigue behaviour of additive manufactured Ti6Al4V, with as-built surfaces, exposed to variable amplitude loading, Int. J. Fatigue vol. 103 (2017) 353–362.
[6] M. Kahlin, H. Ansell, J.J. Moverare, Fatigue behaviour of notched additive manufactured Ti6Al4V with as-built surfaces, Int. J. Fatigue vol. 101 (2017) 51–60.
[7] A. Townsend, N. Senin, L. Blunt, R.K. Leach, J.S. Taylor, Surface texture metrology for metal additive manufacturing: a review, Precis. Eng. vol. 46 (2016) 34–47.
[8] A.S. Wu, D.W. Brown, M. Kumar, G.F. Gallegos, W.E. King, An experimental investigation into additive manufacturing-induced residual stresses in 316L stainless steel, Metall. Mater. Trans. A Phys. Metall. Mater. Sci. vol. 45 (13) (2014) 6260–6270.

[9] E.R. Denlinger, J.C. Heigel, P. Michaleris, T.A. Palmer, Effect of inter-layer dwell time on distortion and residual stress in additive manufacturing of titanium and nickel alloys, J. Mater. Process. Technol. vol. 215 (2015) 123–131.

[10] K. An, L. Yuan, L. Dial, I. Spinelli, A.D. Stoica, Y. Gao, Neutron residual stress measurement and numerical modeling in a curved thin-walled structure by laser powder bed fusion additive manufacturing, Mater. Des. vol. 135 (2017) 122–132.

[11] D. Ma, A.D. Stoica, Z. Wang, A.M. Beese, Crystallographic texture in an additively manufactured nickel-base superalloy, Mater. Sci. Eng. A vol. 684 (September 2016) (2017) 47–53.

[12] N. Nadammal, S. Cabeza, T. Mishurova, T. Thiede, A. Kromm, C. Seyfert, L. Farahbod, C. Haberland, J.A. Schneider, P.D. Portella, G. Bruno, Effect of hatch length on the development of microstructure, texture and residual stresses in selective laser melted superalloy Inconel 718, Mater. Des. vol. 134 (2017) 139–150.

[13] Z. Wang, E. Denlinger, P. Michaleris, A.D. Stoica, D. Ma, A.M. Beese, Residual stress mapping in Inconel 625 fabricated through additive manufacturing: method for neutron diffraction measurements to validate thermomechanical model predictions, Mater. Des. vol. 113 (2017) 169–177.

[14] D. Herzog, V. Seyda, E. Wycisk, C. Emmelmann, Additive manufacturing of metals, Acta Mater. vol. 117 (2016) 371–392.

[15] H.L. Wei, J. Mazumder, T. DebRoy, Evolution of solidification texture during additive manufacturing, Sci. Rep. vol. 5 (2015) 1–7.

[16] D. Deng, J. Moverare, R.L. Peng, H. Söderberg, Microstructure and anisotropic mechanical properties of EBM manufactured Inconel 718 and effects of post heat treatments, Mater. Sci. Eng. A vol. 693 (December 2016) (2017) 151–163.

[17] D. Deng, R.L. Peng, H. Brodin, J. Moverare, Microstructure and mechanical properties of Inconel 718 produced by selective laser melting: sample orientation dependence and effects of post heat treatments, Mater. Sci. Eng. A vol. 713 (December 2017) (2018) 294–306.

[18] J.A. Koepf, M.R. Gotterbarm, M. Markl, C. Körner, 3D multi-layer grain structure simulation of powder bed fusion additive manufacturing, Acta Mater. vol. 152 (2018) 119–126.

[19] R.R. Dehoff, M.M. Kirka, F.A. List, K.A. Unocic, W.J. Sames, Crystallographic texture engineering through novel melt strategies via electron beam melting: Inconel 718, Mater. Sci. Technol. vol. 31 (8) (2015) 939–944.

[20] M.L. Montero-sistiaga, S. Pourbabak, J. Van Humbeeck, D. Schryvers, K. Vanmeensel, Microstructure and mechanical properties of Hastelloy X produced by HP-SLM (high power selective laser melting), Mater. Des. vol. 165 (2019) (2020), 107598.

[21] A. Keshavarzkermani, R. Esmaeilizadeh, U. Ali, P.D. Enrique, Y. Mahmoodkhani, N.Y. Zhou, A. Bonakdar, E. Toyserkani, Controlling mechanical properties of additively manufactured hastelloy X by altering solidification pattern during laser powder-bed fusion, Mater. Sci. Eng. A vol. 762 (May) (2019), 138081.

[22] S. Ghorbanpour, M.E. Alam, N.C. Ferreri, A. Kumar, B.A. McWilliams, S.C. Vogel, J. Bicknell, I.J. Beyerlein, M. Knezevic, Experimental characterization and crystal plasticity modeling of anisotropy, tension-compression asymmetry, and texture evolution of additively manufactured Inconel 718 at room and elevated temperatures, Int. J. Plast. vol. 125 (May 2019) (2020) 63–79.

[23] M.D. Sangid, T.A. Book, D. Naragani, J. Rotella, P. Ravi, A. Finch, P. Kenesei, J. S. Park, H. Sharma, J. Almer, X. Xiao, Role of heat treatment and build orientation in the microstructure sensitive deformation characteristics of IN718 produced via SLM additive manufacturing, Addit. Manuf. vol. 22 (April) (2018) 479–496.

[24] S. Bahl, S. Mishra, K.U. Yazar, I.R. Kola, K. Chatterjee, S. Suwas, Non-equilibrium microstructure, crystallographic texture and morphological texture synergistically result in unusual mechanical properties of 3D printed 316L stainless steel, Addit. Manuf. vol. 28 (December 2018) (2019) 65–77.

[25] L. Kovarik, R.R. Unocic, J. Li, P. Sarosi, C. Shen, Y. Wang, M.J. Mills, Microtwinning and other shearing mechanisms at intermediate temperatures in Ni-based superalloys, Prog. Mater. Sci. vol. 54 (6) (2009) 839–873.

[26] J. Zhao, M. Larsen, V. Ravikumar, Phase precipitation and time – temperature-transformation diagram of Hastelloy X, Mater. Sci. Eng. A vol. 293 (2000) 112–119.

[27] T. DebRoy, H.L. Wei, J.S. Zuback, T. Mukherjee, J.W. Elmer, J.O. Milewski, A. M. Beese, A. Wilson-Heid, A. De, W. Zhang, Additive manufacturing of metallic components – process, structure and properties, Prog. Mater. Sci. vol. 92 (2018) 112–224.

[28] P. Mercelis, J.P. Kruth, Residual stresses in selective laser sintering and selective laser melting, Rapid Prototyp. J. vol. 12 (5) (2006) 254–265.

[29] A. Leicht, C.-H. Yu, V. Luzin, U. Klement, E. Hryha, Effect of scan rotation on the microstructure development and mechanical properties of 316L parts produced by laser powder bed fusion, Mater. Charact. 159 (2020), 110016.

[30] A. Leicht, M. Rashidi, U. Klement, E. Hryha, Effect of process parameters on the microstructure, tensile strength and productivity of 316L parts produced by laser powder bed fusion, Mater. Charact. vol. 159 (November 2019) (2020), 110016.

[31] A. Brule, O. Kirstein, Residual stress diffractometer KOWARI at the Australian research reactor OPAL: status of the project, Phys. B Condens. Matter vol. 385–386 (2006) 1040–1042.

[32] F. Bachmann, R. Hielscher, P.E. Jupp, W. Pantleon, H. Schaeben, E. Wegert, Inferential statistics of electron backscatter diffraction data from within individual crystalline grains, J. Appl. Crystallogr. vol. 43 (6) (2010) 1338–1355.

[33] R. Hielscher, H. Schaeben, A novel pole figure inversion method: specification of the MTEX algorithm, J. Appl. Crystallogr. vol. 41 (6) (2008) 1024–1037.

[34] H.J. Bunge, Some applications of the Taylor theory of polycrystal plasticity, Krist. und Tech. 5 (1970) 145–175.

[35] S. Sjöström, R. Eriksson, S. Johansson, H. Brodin, X.-H. Li, L. Östergren, TBC bond coat–top coat interface roughness: Influence on fatigue life and modelling aspects, Surf. Coat. Technol. vol. 236 (2013) 230–238.

[36] P.J. Withers, H.K.D.H. Bhadeshia, Residual stress part 1 - measurement techniques, Mater. Sci. Technol. vol. 17 (4) (2001) 355–365.

[37] E. Cakmak, T.R. Watkins, J.R. Bunn, R.C. Cooper, P.A. Cornwell, Y. Wang, L. M. Sochalski-Kolbus, R.R. Dehoff, S.S. Babu, Mechanical characterization of an additively manufactured Inconel 718 theta-shaped specimen, Metall. Mater. Trans. A vol. 47 (2) (2016) 971–980.

[38] S. Nath, P. Shukla, X.J. Shen, J. Lawrence, Effect of laser shock peening (LSP) on the phase evolution, residual stress and hardness of Hastelloy-X superalloys, Lasers Eng. vol. 39 (1–2) (2018) 97–112.

[39] D. Dye, S.M. Roberts, P.J. Withers, R.C. Reed, Determination of the residual strains and stresses in a tungsten inert gas welded sheet of IN718 superalloy using neutron diffraction, J. Strain Anal. Eng. Des. vol. 35 (4) (2000) 247–259.

[40] T. Mishurova, K. Artzt, J. Haubrich, G. Requena, G. Bruno, Exploring the correlation between subsurface residual stresses and manufacturing parameters in laser powder bed fused ti-6al-4v, in: Metals, vol. 9, 2019.

[41] L. Thijs, K. Kempen, J.P. Kruth, J. Van Humbeeck, Fine-structured aluminium products with controllable texture by selective laser melting of pre-alloyed AlSi10Mg powder, Acta Mater. vol. 61 (5) (2013) 1809–1819.

[42] L. Thijs, M.L. Montero Sistiaga, R. Wauthle, Q. Xie, J.P. Kruth, J. Van Humbeeck, Strong morphological and crystallographic texture and resulting yield strength anisotropy in selective laser melted tantalum, Acta Mater. 61 (2013) 4657–4668.

[43] S. Sun, T. Ishimoto, K. Hagihara, Y. Tsutsumi, Excellent mechanical and corrosion properties of austenitic stainless steel with a unique crystallographic lamellar microstructure via selective laser melting, Scr. Mater. vol. 159 (2019) 89–93.

[44] W. Kurz, R. Trivedi, Rapid solidification processing and microstructure formation, Mater. Sci. Eng. A vol. 179–180 (PART 1) (1994) 46–51.

[45] D.J.F.W. Kurz, Fundamentals of Solidification, Trans Tech Publications, Zürich, 1998.

[46] D. Rosenthal, The theory of moving sources of heat and its application to metal treatments, Trans. ASME (1946) 849–886.

[47] J. Liu, A.C. To, Quantitative texture prediction of epitaxial columnar grains in additive manufacturing using selective laser melting, Addit. Manuf. vol. 16 (2017) 58–64.

[48] J.D. Hunt, Steady state columnar and equiaxed growth of dendrites and eutectic, Mater. Sci. Eng. vol. 65 (1) (1984) 75–83.

[49] M. Gäumann, C. Bezençon, P. Canalis, W. Kurz, Single-crystal laser deposition of superalloys: processing-microstructure maps,", Acta Mater. vol. 49 (6) (2001) 1051–1062.

[50] C.-H. Yu, R.L. Peng, J.-E. Lundgren, J. Moverare, Anisotropic mechanical properties of thin-walled Hastelloy X manufactured by laser powder bed fusion, in: European Congress and Exhibition on Powder Metallurgy. European PM Conference Proceedings, 2019, pp. 0–5.

[51] T. Ungar, Dislocation densities, arrangements and character from X-ray diffraction experiments, Mater. Sci. Eng. A vol. 310 (A309–310) (2001) 14–22.

[52] S. Das Bakshi, D. Sinha, S. Ghosh Chowdhury, Anisotropic broadening of XRD peaks of α′-Fe: Williamson-Hall and Warren-Averbach analysis using full width at half maximum (FWHM) and integral breadth (IB), Mater. Charact. vol. 142 (March) (2018) 144–153.

[53] W.F. Hosford, Mechanical Behavior of Materials, 2005.

[54] R.W. Kozar, A. Suzuki, W.W. Milligan, J.J. Schirra, M.F. Savage, T.M. Pollock, Strengthening mechanisms in polycrystalline multimodal nickel-base superalloys, Metall. Mater. Trans. A Phys. Metall. Mater. Sci. vol. 40 (7) (2009) 1588–1603.

[55] The mechanism of plastic deformation of crystals. Part I.—Theoretical, in: Proc. R. Soc. London. Ser. A, Contain. Pap. a Math.Phys. Character, 1934.

[56] H. Biermann, M. Strehler, H. Mughrabi, High-temperature measurements of lattice parameters and internal stresses of a creep-deformed monocrystalline nickel-base superalloy, Metall. Mater. Trans. A Phys. Metall. Mater. Sci. 27 (1996) 1003–1014.

[57] T. Ungár, A.D. Stoica, G. Tichy, X.L. Wang, Orientation-dependent evolution of the dislocation density in grain populations with different crystallographic orientations relative to the tensile axis in a polycrystalline aggregate of stainless steel, Acta Mater. vol. 66 (2014) 251–261.

[58] M.R. Staker, D.L. Holt, The dislocation cell size and dislocation density in copper deformed at temperatures between 25 and 700°C, Acta Metall. 20 (1972) 569–579.

[59] H. Mughrabi, A two-parameter description of heterogeneous dislocation distributions in deformed metal crystals, Mater. Sci. Eng. vol. 85 (C) (1987) 15–31.

[60] E. Nes, Modelling of work hardening and stress saturation in FCC metals, Prog. Mater. Sci. vol. 41 (3) (1997) 129–193.

[61] J. Xu, H. Gruber, R. Boyd, S. Jiang, R.L. Peng, J.J. Moverare, On the strengthening and embrittlement mechanisms of an additively manufactured nickel-base superalloy, Materialia 10 (2020), 100657.

[62] W.F. Hosford, The Mechanics of Crystals and Textured Polycrystals, Oxford Univ. Press, 1993.

[63] W.F. Hosford, Mechanical Behavior of Materials, 2005.

[64] G. Chin, W. Mammel, Computer solutions of taylor analysis for axisymmetric flow, Trans. Metall. Soc. AIME (1967).